Magnetic Resonance in Medicine 78:2322–2333 (2017)

Fractional Anisotropy Derived From the Diffusion Tensor Distribution Function Boosts Power to Detect Alzheimer's Disease Deficits

Talia M. Nir,[1] Neda Jahanshad,[1] Julio E. Villalon-Reina,[1] Dmitry Isaev,[1] Artemis Zavaliangos-Petropulu,[1] Liang Zhan,[2] Alex D. Leow,[3] Clifford R. Jack, Jr.,[4] Michael W. Weiner,[5] and Paul M. Thompson,[1]* for the Alzheimer's Disease Neuroimaging Initiative (ADNI)

Purpose: In diffusion MRI (dMRI), fractional anisotropy derived from the single-tensor model (FA^{DTI}) is the most widely used metric to characterize white matter (WM) microarchitecture, despite known limitations in regions with crossing fibers. Due to time constraints when scanning patients in clinical settings, high angular resolution diffusion imaging acquisition protocols, often used to overcome these limitations, are still rare in clinical population studies. However, the tensor distribution function (TDF) may be used to model multiple underlying fibers by representing the diffusion profile as a probabilistic mixture of tensors.

Methods: We compared the ability of standard FA^{DTI} and TDF-derived FA (FA^{TDF}), calculated from a range of dMRI angular resolutions (41, 30, 15, and 7 gradient directions), to profile WM deficits in 251 individuals from the Alzheimer's Disease Neuroimaging Initiative and to detect associations with 1) Alzheimer's disease diagnosis, 2) Clinical Dementia Rating scores, and 3) average hippocampal volume.

Results: Across angular resolutions and statistical tests, FA^{TDF} showed larger effect sizes than FA^{DTI}, particularly in regions preferentially affected by Alzheimer's disease, and was less susceptible to crossing fiber anomalies.

Conclusion: The TDF "corrected" form of FA may be a more sensitive and accurate alternative to the commonly used FA^{DTI}, even in clinical quality dMRI data. **Magn Reson Med 78:2322–2333, 2017. © 2017 International Society for Magnetic Resonance in Medicine.**

Key words: Alzheimer's disease; white matter; diffusion-weighted imaging; fractional anisotropy; tensor distribution function

INTRODUCTION

Diffusion-weighted MRI (dMRI) is a variant of standard MRI that can measure the diffusion of water molecules in biological tissues, such as the brain. By characterizing the diffusion process at the voxel level, we can make tentative inferences about the underlying white matter (WM) microstructure and factors that affect it (1). Since dMRI was developed, acquisition protocols have improved to increase angular, spatial, and spectral resolution. Multiple mathematical models have been developed to describe the diffusion process. One of the first—and still most popular—methods of summarizing diffusion properties in a specific voxel is the single tensor model (2), commonly referred to as diffusion tensor imaging (DTI) (3). This model is limited because it assumes diffusion is purely Gaussian; it can only model a single fiber population, with a single dominant orientation, at every voxel. It cannot resolve complex WM architecture, such as dispersing, crossing, or kissing fibers. Yet, at the current resolution of dMRI, between one third and two thirds of WM voxels contain fiber crossings (4,5). dMRI can also be used to evaluate disease-related gray matter (GM) abnormalities, where the microarchitecture is even more complex (6). Nevertheless, the tensor-derived fractional anisotropy (FA^{DTI}) metric is still the most widely used scalar measure to characterize tissue microarchitecture. It is widely used in research studies of schizophrenia, depression, autism, HIV/AIDS, and other developmental, psychiatric, and neurodegenerative disorders, including Alzheimer's disease (AD) (7,8).

In recent years, many new models have been proposed to overcome limitations of the tensor model, including *q*-ball imaging and diffusion orientation distribution functions (ODFs) (9), constrained spherical deconvolution (10), diffusion spectrum MRI (11), multicompartment models such as the ô"ball and stick"ô model (4), and neurite orientation dispersion and density imaging (NODDI) (12). Due to the numerous types of biological, neuropsychiatric, and imaging data often acquired for clinical populations, time constraints are often placed on imaging protocols to reduce patient attrition or motion and ensure adequate sample sizes. This currently precludes state of the art models such as NODDI and those derived from diffusion spectrum MRI, which require extremely dense or multishell acquisitions, and may

---

[1]Imaging Genetics Center, University of Southern California, Marina del Rey, California, USA.
[2]Computer Engineering Program, University of Wisconsin-Stout, Menomonie, Wisconsin, USA.
[3]Department of Psychiatry and Bioengineering, University of Illinois, Chicago, Illinois, USA.
[4]Department of Radiology, Mayo Clinic and Foundation, Rochester, Minnesota, USA.
[5]Department of Radiology, University of California San Francisco School of Medicine, San Francisco, California, USA.

*Correspondence to: Paul Thompson, Imaging Genetics Center, 4676 Admiralty Way, Suite 200, Marina del Rey, CA 90292. E-mail: pthomp@usc.edu

Received 15 June 2016; revised 21 November 2016; accepted 8 January 2017
DOI 10.1002/mrm.26623

prevent the reliable reconstruction of many other higher-order diffusion models. However, the tensor distribution function (TDF), as proposed by Leow et al (13), may still be feasible. The TDF is a probabilistic extension of a multitensor model that describes crossing fibers mathematically as an ensemble of Gaussian tensors. However, unlike other multicompartment models (4,12,14–16) in which one needs to specify in advance the total number of compartments in the tissue, the authors propose a continuous distribution of tensors, with a profile of "weights" or relative contributions estimated for tensors with a continuously varying range of shapes and sizes in the tensor space.

The Alzheimer's Disease Neuroimaging Initiative (ADNI) is a large, longitudinal, multisite study of healthy elderly controls, individuals with mild cognitive impairment, and AD. The goal is to identify sensitive imaging biomarkers that can be used to track or predict changes in the brain, which is vital for drug trials to identify candidates for treatment and monitor effectiveness. In addition to the battery of cognitive tests, cerebrospinal fluid and blood tests, the ADNI collects several functional and structural MRI modalities, including T1- and T2-weighted anatomical MRI, positron emission tomography, arterial spin labeling, resting state functional MRI, and dMRI. In such longitudinal studies, there is a real concern about patient attrition, especially in elderly individuals who may not be able to tolerate being confined to a scanner for long periods. In an effort to collect such a wide range of data types and maintain patient enrollment, time constraints are placed on possible dMRI protocols, including debates as to whether or not to continue acquiring dMRI in the next phase of the ADNI. Clearly it is of great interest to maximize the power of the available scans and show that even clinical quality diffusion scans can be powerful tools for uncovering disease-related abnormalities in tissue microstructure and WM neurocircuitry.

The goal of this study was to determine whether FA metrics derived using the TDF model (FA^{TDF}) may be more sensitive to disease-related differences than the corresponding FA^{DTI} measure that is now widely used. Building on preliminary findings reported by Nir et al (17), our goal was to understand how the imaging protocol may influence the sensitivity of the FA metrics, and further compared performance for each metric computed from subsamples of the full ADNI dMRI 41 gradient direction angular resolution, including subsets of 30, 15, and 7 gradient directions. Voxel-wise association tests were used to compare FA^{TDF} and FA^{DTI} metrics computed from a range of angular resolutions and their ability to detect microstructural differences between AD patients and healthy elderly controls. We also evaluated associations between the two FA metrics and common AD biomarkers—hippocampal volume and Clinical Dementia Rating (CDR) scores. Finally, we evaluated the test/retest reliability of each model's fit and the resulting scalar FA maps. In comparing models, there is interest in detecting clinical associations with maximal sensitivity and power, ideally using improved metrics, which measure standard properties more accurately.

METHODS

Subjects and Image Acquisition

Standard MRI, dMRI, and clinical data were downloaded from the publicly available ADNI database (www.loni.usc.edu/ADNI). We analyzed baseline data from 251 participants: 53 healthy controls (mean age, 72.6 ± 6.1 y; men, n = 24; women, n = 29), 28 with significant memory concern (mean age, 72.4 ± 4.5 y; men, n = 10; women, n = 18), 121 with mild cognitive impairment (mean age, 72.6 ± 7.3 y; men, n = 75; women, n = 46) and 49 with AD (mean age, 75.0 ± 8.6 y; men, n = 29; women, n = 20). Of the 53 control participants, 33 returned for follow-up evaluations after 3 months, and their scans were used for test/retest analyses (mean age, 72.8 ± 6.5 y; men, n = 16; women, n = 17). All procedures were reviewed and approved by institutional review boards. All participants gave written informed consent.

All subjects underwent whole brain MRI scanning on 3T GE Medical Systems scanners at 17 acquisition sites across North America. Anatomical T1-weighted spoiled gradient echo sequences (matrix = 256×256; voxel size = $1.2 \times 1.0 \times 1.0\,\text{mm}^3$; TI = 400 ms; TR = 6.98 ms; TE = 2.85 ms; flip angle = 11°) and dMRI (matrix = 128×128; voxel size = $2.7 \times 2.7 \times 2.7\,\text{mm}^3$; TR = 9000 ms; dMRI scan time = 9 min) were collected. A total of 46 separate images were acquired for each dMRI scan: 5 T2-weighted images with no diffusion sensitization (b_0 images) and 41 diffusion-weighted images (DWI; $b = 1000\ \text{s/mm}^2$).

Baseline hippocampal volume summary metrics, processed using the FreeSurfer package (http://surfer.nmr.mgh.harvard.edu), were downloaded from the ADNI database (n = 243 available), as was the sum-of-boxes Clinical Dementia Rating score (CDR-sob; n = 238) (18).

Image Preprocessing

Raw images were preprocessed as described by Nir et al. (7). Extracerebral tissue was removed, raw DWI images were corrected for motion and eddy current distortions, and T1-weighted images underwent inhomogeneity normalization. Each T1-weighted image was linearly aligned to a standard brain template. The diffusion images were linearly and then elastically registered (19) to their respective T1-weighted scans to correct for echo planar imaging–induced susceptibility artifacts. Gradient tables were corrected for DWI linear registrations.

Diffusion Gradient Subsampling

To gain a better understanding of the dMRI parameters necessary to employ the TDF model, we used the framework presented by Zhan et al. (20) to "downsample" the angular resolution from 41 gradient directions to include only a subset of either 30, 15, or 7 gradient images. Gradient subsets were selected by optimizing the spherical angular distribution energy. Briefly, the angular distribution energy, E_{ij}, of a pair of points, i and j, on the unit sphere may be defined as the inverse of the sum of the squares of (1) the least spherical distance between point i and point j, and (2) the least spherical distance between point i and point j's antipodal, symmetric point J. As in previous work, we acknowledge that protocols with fewer gradients would be independently optimized for angular distribution rather than subsample directions from an existing protocol, but the subsampling we use is designed to lead to the most equally distributed sampling on the sphere possible. It also helps us to assess effects of gradient count while keeping other factors of the patient's scan constant (e.g., motion, artifacts).

dMRI Reconstruction Models and Scalar Maps

For each angular resolution (41, 30, 15, or 7 gradient directions), three different dMRI reconstruction models were used to generate scalar FA maps. First, a single diffusion tensor (3)—equivalent to a 3D ellipsoid capturing a single fiber orientation—was modeled at each voxel in the brain from the corrected DWI scans. This model assumes that the diffusion is a 3D Gaussian process, fitted using just six independent parameters of a tensor (3 eigenvalues describing its shape, and 3 Euler angles describing its orientation). Scalar fractional anisotropy (FA^{DTI}) maps were obtained from the resulting diffusion tensor eigenvalues (λ_1, λ_2, λ_3):

$$FA = \sqrt{\frac{(\lambda_1-\lambda_2)^2+(\lambda_1-\lambda_3)^2+(\lambda_2-\lambda_3)^2}{2[\lambda_1^2+\lambda_2^2+\lambda_3^2]}}$$

In contrast to the single tensor model, the tensor distribution function (TDF) represents the diffusion profile as a probabilistic mixture of tensors that optimally explain the observed DWI data, allowing for the reconstruction of multiple underlying fibers per voxel, together with a distribution of weights or probabilities. We applied the framework proposed by Leow et al. (13) and Zhan et al. (21) to the angular diffusion signal to compute the voxel-wise optimal TDF, $P^*(D(\theta, \lambda))$—the probability distribution function of all feasible Gaussian tensors $D(\theta, \lambda)$ that best describes the observed signal. As described by Leow et al., to reduce the solution space, each tensor $D(\theta, \lambda)$ at spherical angle θ was assumed to be cylindrical such that $\lambda = (\lambda_1, \lambda_2 = \lambda_3)$ and $\lambda_1 \geq \lambda_2$. However, unlike the gradient descent approach used by Leow et al. to solve for this optimal TDF, we used a quadratic programming approach (see Appendix for details). The tensor orientation distribution function (TOD) was then calculated by computing the marginal density function of the TDF with the eigenvalues $\lambda = (\lambda_1, \lambda_2)$ integrated out.

$$TOD(\theta) = \int_\lambda P\Big(D(\theta,\lambda)\Big)d\lambda$$

For each θ, the eigenvalues are calculated by computing the expected value of each eigenvalue along θ, from which a corresponding scalar FA metric is calculated:

$$\lambda_i'(\theta) = \frac{\int P\Big(D(\theta,\lambda)\Big)\lambda_i d\lambda}{\int P\Big(D(\theta,\lambda)\Big)d\lambda}$$

$$FA(\theta) = \sqrt{\frac{(\lambda_1'(\theta)-\lambda_2'(\theta))^2+(\lambda_1'(\theta)-\lambda_3'(\theta))^2+(\lambda_2'(\theta)-\lambda_3'(\theta))^2}{2[\lambda_1'(\theta)^2+\lambda_2'(\theta)^2+\lambda_3'(\theta)^2]}}$$

At each voxel, the final scalar FA^{TDF} metric across all θ is then calculated as the sum of all $FA(\theta)$ weighted by the probability that θ is the principal fiber direction, $TOD(\theta)$.

$$FA^{TDF} = \int TOD(\theta) * FA(\theta) d\theta$$

A healthy control subject's FA^{DTI} and FA^{TDF} maps, calculated from various angular resolutions, are shown in Figure 1a and 1b for visual comparison. A voxel-wise, two-tailed, paired *t* test was performed to quantitatively compare TDF and DTI FA values in the healthy control group. All resulting statistical maps were corrected for multiple comparisons using the standard false discovery rate (FDR) method at $q = 0.05$ (22) and thresholded at the FDR critical *P* value.

For comparison to an established high angular resolution diffusion imaging technique also designed to reconstruct multiple fiber orientations in a given voxel, we fitted ODFs at each voxel, with a nonparametric *q*-ball reconstruction technique, using the normalized and dimensionless constant solid angle (CSA) method (9,23). The generalized FA (GFA^{ODF}) was then calculated from the CSA-ODF. GFA^{ODF} is analogous to FA^{DTI}, but calculated at each diffusion direction of the ODF (9) and is defined as:

$$GFA = \frac{std(\Psi)}{rms(\Psi)} = \sqrt{\frac{n\sum_{i=1}^{n}\Big(\Psi(u_i)-\Psi\Big)^2}{(n-1)\sum_{i=1}^{n}\Psi(u_i)^2}}$$

Here, $\Psi(u)$ is the ODF, i is each diffusion direction, and $\Psi = \frac{1}{n}\sum_{i=1}^{n}\Psi(u_i)$ is the mean of the ODF.

Template Creation and Spatial Normalization

To avoid bias in the diffusion-based registrations, we created a multichannel, study-specific minimal deformation template with the ANTs registration software (24), equally weighting FA^{DTI}, FA^{TDF}, GFA^{ODF} and T1-weighted maps. Similarly, to spatially normalize each subject's three FA maps, we performed a three-channel linear then nonlinear registration to the minimal deformation template. In this way, all FA maps were used to drive the registration, and they were all normalized to the same space. To avoid differences in registration accuracy, the deformations from the full angular resolution registration were applied to the FA maps calculated from the various DWI gradient subsets for each individual.

Test/retest FA^{DTI} and FA^{TDF} maps generated from baseline and 3-month follow-up dMRI scans were each linearly aligned to an intermediate space halfway between each subject's two time points (25). Baseline and follow-up maps were each spatially normalized to the baseline minimal deformation template with two-channel linear then nonlinear registrations. The deformations from the full angular resolution registration were

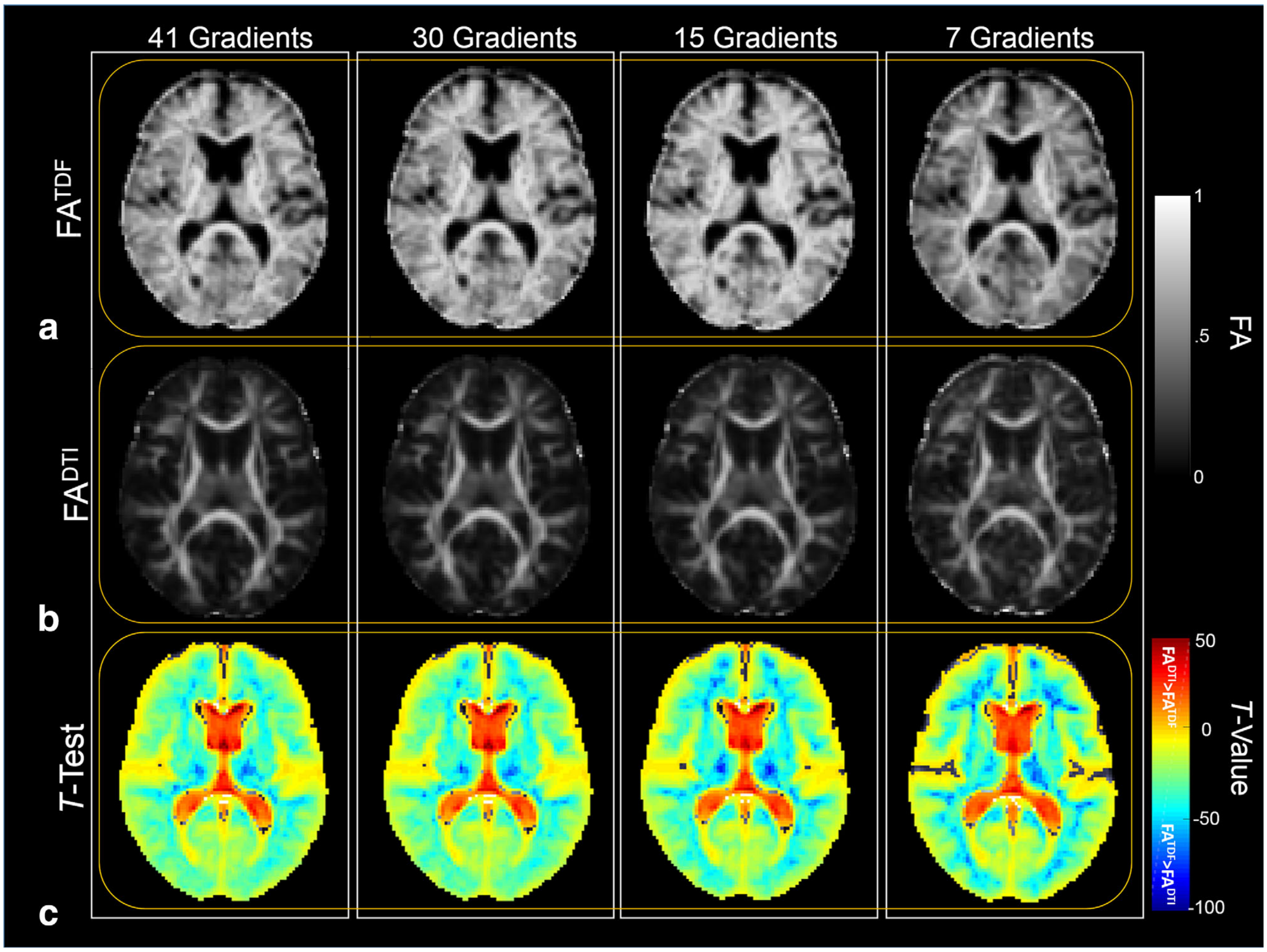

FIG. 1. Diffusion FA maps, (**a**) FA^{TDF} and (**b**) FA^{DTI}, are shown for a single subject calculated from 41, 30, 15, and 7 gradient direction sets. The FA^{TDF} maps show more sharply defined WM boundaries, with much less signal dropout in regions near the cortex that tend to have less coherent WM, compared with FA^{DTI} maps. (**c**) *t* test maps in regions where FA^{DTI} and FA^{TDF} maps are significantly different reveal lower FA^{DTI} values (negative association) throughout the tissue regardless of angular resolution (FDR critical *P* value for 41 gradients = 0.047, 30 gradients = 0.047, 15 gradients = 0.047, and 7 gradients = 0.046).

applied to the various test/retest DWI gradient subsets as well as the respective FA maps.

Clinical Associations and Effect Sizes

To test for statistical effects of AD diagnosis on measures of white matter microstructure–FA^{DTI}, FA^{TDF}, and GFA^{ODF} maps calculated at various angular resolutions–we ran voxel-wise, random-effects linear regressions, covarying for age and sex, and using the acquisition site as the random grouping variable. In an effort to try and tease apart microstructural associations from those driven by atrophy and registration, for each voxel, we also covaried for the log Jacobian determinant derived from the nonlinear spatial normalization of each map to the template. In addition to AD diagnosis, we also tested for voxel-wise associations between FA and CDR-sob scores as well as average bilateral hippocampal volume (after covarying for intracranial volume) across the entire study sample. All statistical tests were limited to voxels present in all subject scans, as some scans had a slightly cropped field of view. As such, we did not consider the inferior parts of the cerebellum and brain stem. All resulting statistical maps were corrected for multiple comparisons using the standard FDR method at $q = 0.05$ (22), and thresholded at the FDR critical *P* value. We show regression coefficients (β values) only in regions where the false discovery rate was controlled.

We computed cumulative distribution function (CDF) plots to visualize and rank effect sizes across voxel-wise tests. The sorted observed voxel *P* values from each regression were plotted against the *P* values from the expected null distribution. If the CDF curve initially rises at a rate steeper than 20 times the null CDF ($y = 20x$), then the corresponding maps have suprathreshold or FDR significant voxels at $q = 0.05$. Curves that rise at a steeper rate than that line represent significant voxels and larger deviations represent larger effect sizes.

Effect sizes for detecting AD versus control group differences were also compared using Cohen's *d* calculated as $(\mu_{AD} - \mu_{CN})/s_{pooled}$, where $s_{pooled} = \sqrt{[(s_{CN}^2 + s_{AD}^2)/2]}$ (26). This metric has been widely used in studies of disease effects on imaging measures (27–29). For each FA

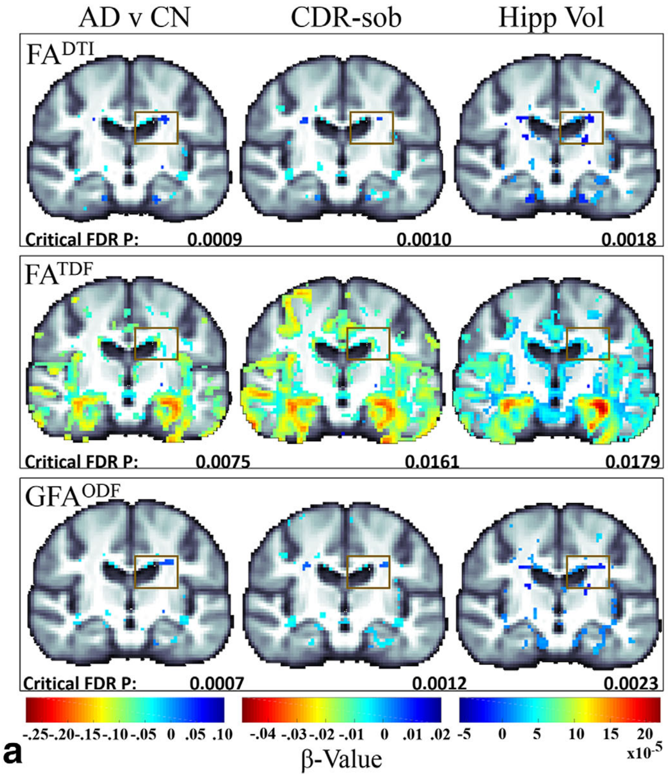

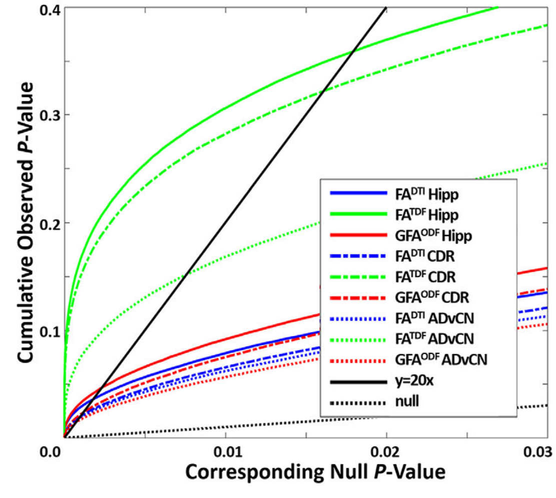

	AD v CN	Hipp Vol	CDR-sob
FA^{TDF}	0.22% (59)	0.18% (117)	0.15% (88)
GFA^{ODF}	10.29% (269)	9.13% (769)	8.17% (348)
FA^{DTI}	13.60% (441)	14.80% (949)	14.20% (506)

c

FIG. 2. (**a**) β maps show regions where lower FA^{DTI}, FA^{TDF}, and GFA^{ODF} is significantly associated with AD diagnosis, higher CDR-sob cognitive deficits, and lower average bilateral hippocampal volume. Across tests, FA^{TDF} maps (middle row) consistently show larger effect sizes in temporal lobe and hippocampal regions. This is denoted by greater β value magnitudes and more pervasive significant associations. The patterns are also more in line with the expected topography of the disease effects. (**b**) CDF plots show effect sizes for FA^{DTI}, FA^{TDF}, and GFA^{ODF} statistical associations. FA^{TDF} maps (green lines) are consistently the most sensitive metric (denoted by the higher critical *P* values controlling the FDR [i.e., the highest nonzero *x*-coordinate where the CDF crosses the $y = 20x$ line]). (**c**) The absolute number and percentage of total significant voxels surviving FDR correction, showing an association direction opposite to that traditionally accepted as showing impairment (dark blue voxels highlighted by boxes in panel a). FA^{DTI} and GFA^{ODF} associations show ~8%-15%, whereas FA^{TDF} tests show $< 0.5\%$, suggesting that FA^{TDF} may be handling computations better in areas with crossing fibers.

metric and angular resolution, we used the average FA from the respective statistical test's significant cluster. To avoid overfitting, a 10-fold cross-validation approach was used. In each fold, 80% of the data were used for voxel-wise regressions to estimate the significant clusters (training data), and the remaining test data were used to compute the Cohen's *d* effect sizes.

Test/Retest Reliability and Model Fit

We used the framework defined by Rokem et al. (30) and Pestilli et al. (31) to evaluate the goodness of the fit of each dMRI model in healthy controls. We first compared the voxel-wise root mean squared error (RMSE) between the observed signal (A) and expected signal (B) from each model in each voxel:

$$\mathrm{RMSE}(A,B) = \sqrt{\frac{\sum_{i=1}^{N}(A_i - B_i)^2}{N}},$$

where N is the number of gradient directions or DWIs and A_i, B_i are the observed and expected signal intensities in the given voxel in the *i*-th DWI. Additionally, baseline and 3-month follow-up test/retest data were used to cross-validate each model's fit—the model parameters were first estimated on baseline control subjects' DWI scans, and then used to predict the signal in the 3-month follow-up DWI scan. As proposed by Rokem et al., we defined the test/retest relative RMSE (rRMSE) in each voxel as

$$\mathrm{rRMSE} = \frac{\left(\mathrm{RMSE}(M1,D2) + \mathrm{RMSE}(M2,D1)\right)}{2\mathrm{RMSE}(D1,D2)}.$$

Here, RMSE(M1,D2) is the RMSE between the data observed in the follow-up scan and predicted from the first scan, RMSE(M2,D1) is the RMSE between the observed data in the first scan and that predicted from the follow-up scan, and RMSE(D1,D2) is the RMSE between the observed data from both scans. A model that predicts the repeated measurement more accurately than the original will result in an $\mathrm{rRMSE} < 1$ (30). To compute RMSE (M1,D2), we used parameters learned from the first scan, and the bvecs (scanner gradient directions) and b_0 from the follow-up scan, and vice versa for RMSE(M2,D1). A voxel-wise two-tailed paired *t* test was performed to compare TDF and DTI baseline RMSE and rRMSE values in the healthy control group.

Table 1
Comparison of FA^{DTI} and FA^{TDF} Statistical Effect Sizes

	FDR Critical *P* Value				Surviving Voxels				Surviving Voxels with Opposite Association			
Gradients	41	30	15	7	41	30	15	7	41	30	15	7
AD vs. controls												
FA^{TDF}	0.0076	0.0085	0.0099	0.0105	15.17%	16.99%	19.83%	20.91%	0.22% (59)	0.17% (53)	0.10% (34)	0.16% (59)
FA^{DTI}	0.0009	0.0008	0.0005	0.0004	1.80%	1.63%	1.07%	0.71%	13.60% (441)	13.75% (404)	13.43% (259)	5.92% (76)
Average hippocampal volume												
FA^{TDF}	0.0179	0.0208	0.0208	0.0165	35.88%	41.57%	41.53%	32.99%	0.18% (117)	0.14% (101)	0.10% (76)	0.17% (98)
FA^{DTI}	0.0018	0.0018	0.0014	0.0006	3.56%	3.65%	2.80%	1.21%	14.80% (949)	13.81% (909)	13.91% (701)	10.11% (220)
CDR-sob												
FA^{TDF}	0.0161	0.0167	0.0177	0.0180	32.18%	33.42%	35.48%	36.00%	0.15% (88)	0.16% (97)	0.13% (80)	0.18% (117)
FA^{DTI}	0.0010	0.0009	0.0005	0.0004	1.98%	1.82%	1.05%	0.88%	14.20% (506)	14.27% (468)	13.70% (260)	4.52% (72)

Comparison is based on the FDR critical *P* value and percent of voxels surviving FDR (22) for the full 41 gradients angular resolution and each of the 30, 15, and 7 gradient subsets, followed by the absolute number and percent of total significant voxels surviving FDR correction, showing an association direction opposite to that traditionally accepted as showing impairment (i.e., higher FA with increased deficits).

All resulting statistical maps were corrected for multiple comparisons using the standard FDR method at $q = 0.05$ (22); resulting maps were thresholded at the FDR critical *P* value.

We also evaluated the test/retest reliability for FA^{DTI} and FA^{TDF} maps calculated from each angular resolution by computing the voxel-wise intraclass correlation (ICC) between baseline and 3-month follow-up healthy control FA maps, with the R PSYCH package (personality-project.org/r/html/ICC.html). Again, the FDR method was used to correct for multiple comparisons.

RESULTS

Both a visual comparison of FA^{DTI} and FA^{TDF} maps (Fig. 1a and 1b) and *t* test between maps (Fig. 1c) reveal that FA^{TDF} maps have higher FA values not only in the core, coherent WM structures but throughout the tissue, including near GM/WM boundaries. The standard FA^{DTI} measure tends to show loss of signal near cortical boundaries and in regions with known fiber crossings and complex gray matter architecture.

Clinical Associations and Effect Sizes

As expected, across all of the FA metrics, AD diagnosis, greater cognitive impairment (higher CDR-sob score), and lower average hippocampal volume were associated with significant WM deficits (lower FA) after correction for multiple comparisons (Fig. 2a). However, across statistical tests, larger effect sizes, as denoted by greater β value magnitude and more widespread differences, were detected with FA^{TDF} voxel maps compared with FA^{DTI} and GFA^{ODF}. Moreover, FA^{TDF} findings are highly localized to the temporal lobe and hippocampal regions most vulnerable to early changes in AD. CDF plots further reflect the increased sensitivity of FA^{TDF} for differentiating disease groups, and for detecting clinical associations (Fig. 2b).

Across maps, some very small regions exhibited significant associations with FA in a direction contrary to what would traditionally be accepted as showing impairment (i.e., higher FA with impairment; Fig. 2a, boxed regions). These regions were largely found at the junction of the corpus callosum commissural fibers and the *corona radiata*, a region notorious for fiber crossings that may reduce the FA, as computed from the tensor model (32). However, across analyses, FA^{TDF} showed fewer associations that were contrary to the hypothesized effects of the disease (Fig. 2c). Relative to the total number of significant voxels, FA^{DTI} showed between ~13% and 15% of these voxels, GFA^{ODF} showed between ~8% and 10%, and FA^{TDF} showed < 0.5% across tests, suggesting that FA^{TDF} may be handling computations better for crossing fibers.

A comparison of the same three clinical associations with FA^{DTI} and FA^{TDF} computed from a subset of 30, 15, and 7 gradient directions revealed that even at 7 gradient directions, FA^{TDF} was consistently the most sensitive metric across statistical tests (Table 1, Fig. 3). In fact, FA^{TDF} calculated from 7 gradient directions had larger effect sizes than FA^{DTI} calculated at the full angular resolution. Across statistical tests performed at each angular

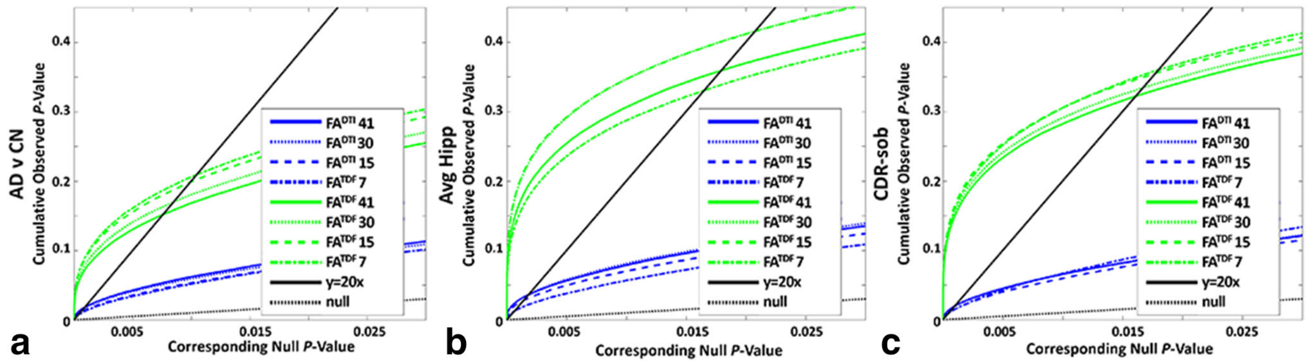

FIG. 3. CDF plots of statistical associations between (**a**) AD diagnosis, (**b**) average bilateral hippocampal volume, and (**c**) CDR-sob and FA^{DTI} or FA^{TDF} maps computed from 41, 30, 15, and 7 gradient direction sets. FA^{TDF} maps (green lines) are consistently the most sensitive metric (denoted by the higher critical *P* values controlling the FDR [i.e., the highest nonzero *x*-coordinate where the CDF crosses the $y = 20x$ line]) across all gradient subsets. Curves correspond to values listed in Table 1.

resolution, FA^{TDF} consistently showed less than 0.5% of significant voxels with a direction of association opposite to that hypothesized, compared with FA^{DTI} which showed between ~5% and 15% (Table 1). Finally, the mean Cohen's *d* effect sizes for picking up AD versus control group differences—which were calculated using test data from the 10-fold cross-validation—once again confirmed that across all angular resolutions, FA^{TDF} showed larger effect sizes (Table 2).

Test/Retest Reliability and Model Fit

Mean maps of the RMSE calculated from the DTI and TDF model fit in the subset of 53 healthy control subjects are shown in Figure 4a and 4b. A voxel-wise *t* test revealed significantly lower error in the TDF fit throughout the tissue regardless of angular resolution (Fig. 5a; FDR critical *P* value for 41 gradients = 0.041, 30 gradients = 0.041, 15 gradients = 0.042, and 7 gradients = 0.043). The mean rRMSE maps from DTI and TDF models from 33 healthy control individuals at two time points are shown in Figure 4c and 4d. While the rRMSE was high in both the TDF and DTI models in the superior cortical gray matter (mean rRMSE > 1), the fit was stable (< 1) in WM and overall temporal lobe regions where most of the AD-related effects were detected. A *t* test between the DTI and TDF rRMSE maps (Fig. 5b) revealed significantly lower rRMSE for the TDF fit, in not only the temporal lobes, but in the region of the superior WM where commissural fibers and the corona radiata intersect, often leading to depleted FA^{DTI}. The TDF model showed higher error only in cerebrospinal fluid. TDF rRMSE was progressively more similar to DTI (i.e., less area of significant differences) with lower angular resolution (FDR critical *P* value for 41 gradients = 0.024, 30 gradients = 0.021, 15 gradients = 0.017, and 7 gradients = 0.001).

In terms of test/retest reliability of the scalar FA maps, we found that across resolutions there was an overall stable and strong ICC between baseline and follow-up FA^{TDF} maps (mean ICC ~0.8; Fig. 5c), whereas, as might be expected, there was a degradation in FA^{DTI} ICC at the lowest angular resolutions (Fig. 5d).

DISCUSSION

FA metrics derived from the tensor distribution function (TDF) may be more sensitive to disease-related microstructural abnormalities than corresponding single tensor-derived FA metrics that are now widely used to assess clinical data. FA is highly affected by numerous factors, including the number of dominant fiber directions and orientation coherence as well as partial volume effects from neighboring GM. By using the TDF approach, we can still employ an extension of the tensor model, adapted to identify contributions to FA from separate crossing fiber compartments in tissue with more complex microarchitecture and in voxels on tissue boundaries that are susceptible to partial voluming.

AD is characterized by cortical and hippocampal neuronal loss and widespread GM atrophy driven in part by cortical amyloid plaque, neurofibrillary tangle deposits, and vascular changes. Structural and diffusion MRI studies show WM injury, perhaps due to myelin degeneration, and neuronal loss leading to progressive disconnection of cortical and subcortical regions (7,33–36). Standard anatomical MRI is still the imaging technique most often used in AD studies and clinical trials, but dMRI is sensitive to microscopic changes in WM integrity not always detectable with standard anatomical MRI (37,38). In addition to WM, dMRI is an emerging tool for the evaluation of disease-related GM abnormalities as well (6,39–43). A growing number of studies are assessing cortical and subcortical GM diffusivity changes in AD that may reflect GM cellular microstructure breakdown (6). Several studies report microscopic changes in

Table 2
Mean Cohen's *d* Effect Sizes Across 10 Folds for Picking Up FA^{DTI} and FA^{TDF} Group Differences Between AD Patients and Healthy Controls Across Angular Resolutions

Gradients	FA^{DTI}	FA^{TDF}
41	1.64 (0.11)	1.90 (0.06)
30	1.63 (0.14)	1.88 (0.06)
15	1.64 (0.15)	1.87 (0.07)
7	1.77 (0.39)	1.95 (0.08)

All data are presented as the mean (standard deviation).

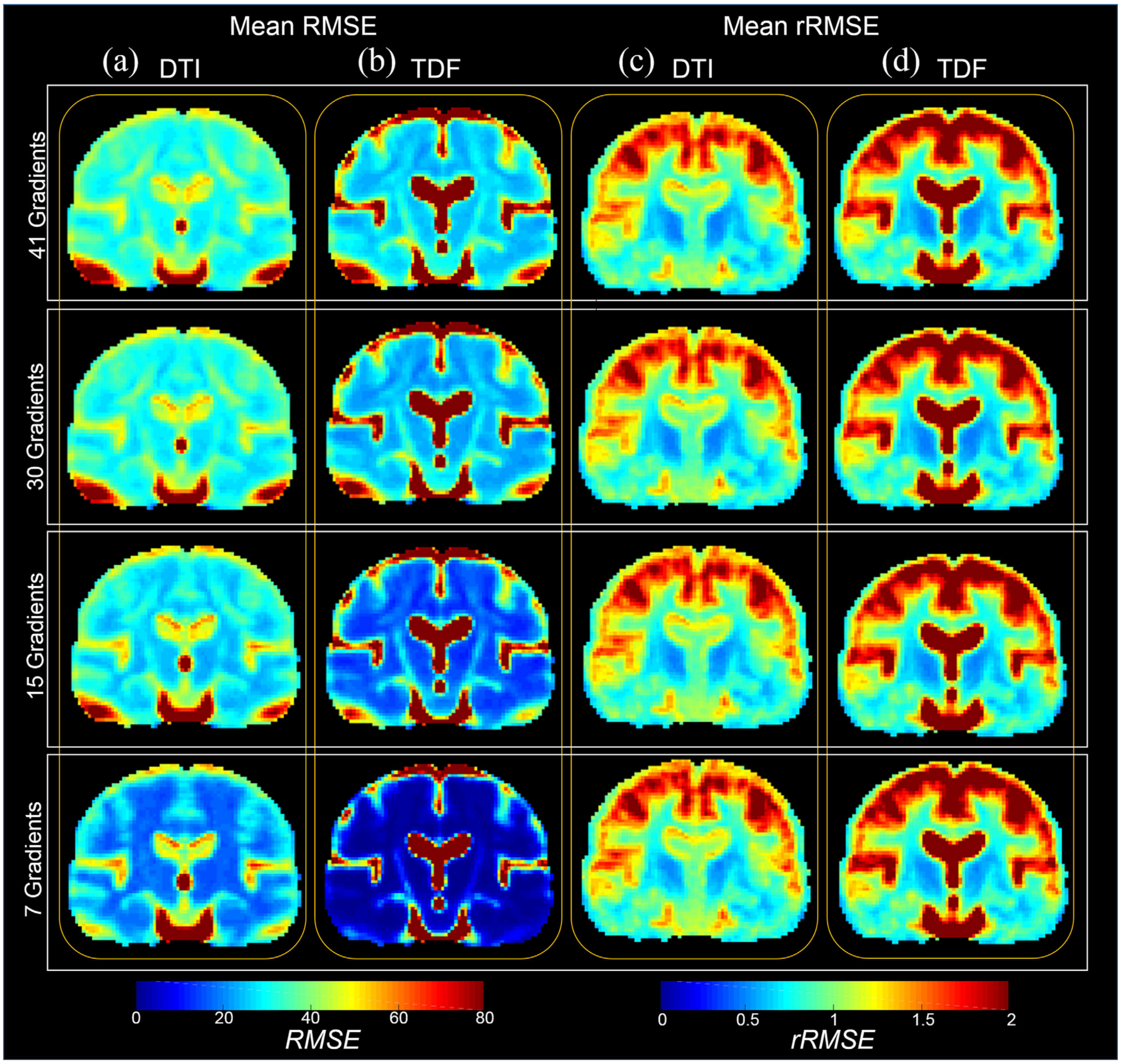

FIG. 4. The left two columns show the root mean squared error (RMSE) maps from the (**a**) DTI and (**b**) TDF model fit, averaged across 53 healthy control subjects. The right two columns show the rRMSE maps from the (**c**) TDF and (**d**) TDF model fit, trained on baseline scans and tested on 3-month follow-up scans in each of 33 control subjects individually, and averaged across the group.

the hippocampi that may be detectable prior to volumetric changes (43,44). Because dMRI changes may be detectable before (and therefore predict) gross volume loss (45,46), it is important to maximize the power to detect such changes.

In this study, we found that compared with both GFA^{ODF} and FA^{DTI}, FA^{TDF} showed increased power to detect subtle or diffuse disease effects, especially in hippocampal and temporal lobe regions. AD pathology targets GM regions, especially in the temporal lobe and hippocampus. In these regions, FA^{DTI} might be suboptimal, as it is best suited to detect differences in cohesive WM fiber bundles (e.g., the corpus callosum). We also found more significant FA^{TDF} associations in voxels at GM or cerebrospinal fluid boundaries that may otherwise be susceptible to partial volume effects with FA^{DTI}. Compared with FA^{DTI}, larger FA^{TDF} effect sizes were preserved even when the dMRI angular resolution was subsampled from 41 gradient directions to 30, 15, or even 7 gradient directions. Perhaps surprisingly, FA^{TDF} calculated from 7 gradient directions had larger effect sizes than FA^{DTI} calculated at the full angular resolution. Whereas some higher-order models require extremely dense or multishell acquisitions, TDF may better extract the information typically available in clinical settings, where time constraints limit scan times. It may also be helpful for studies of valuable but lower-resolution legacy data. The TDF as proposed by Leow et al. (13) makes no assumptions about the number of compartments per voxel and, unlike the tensor distribution function

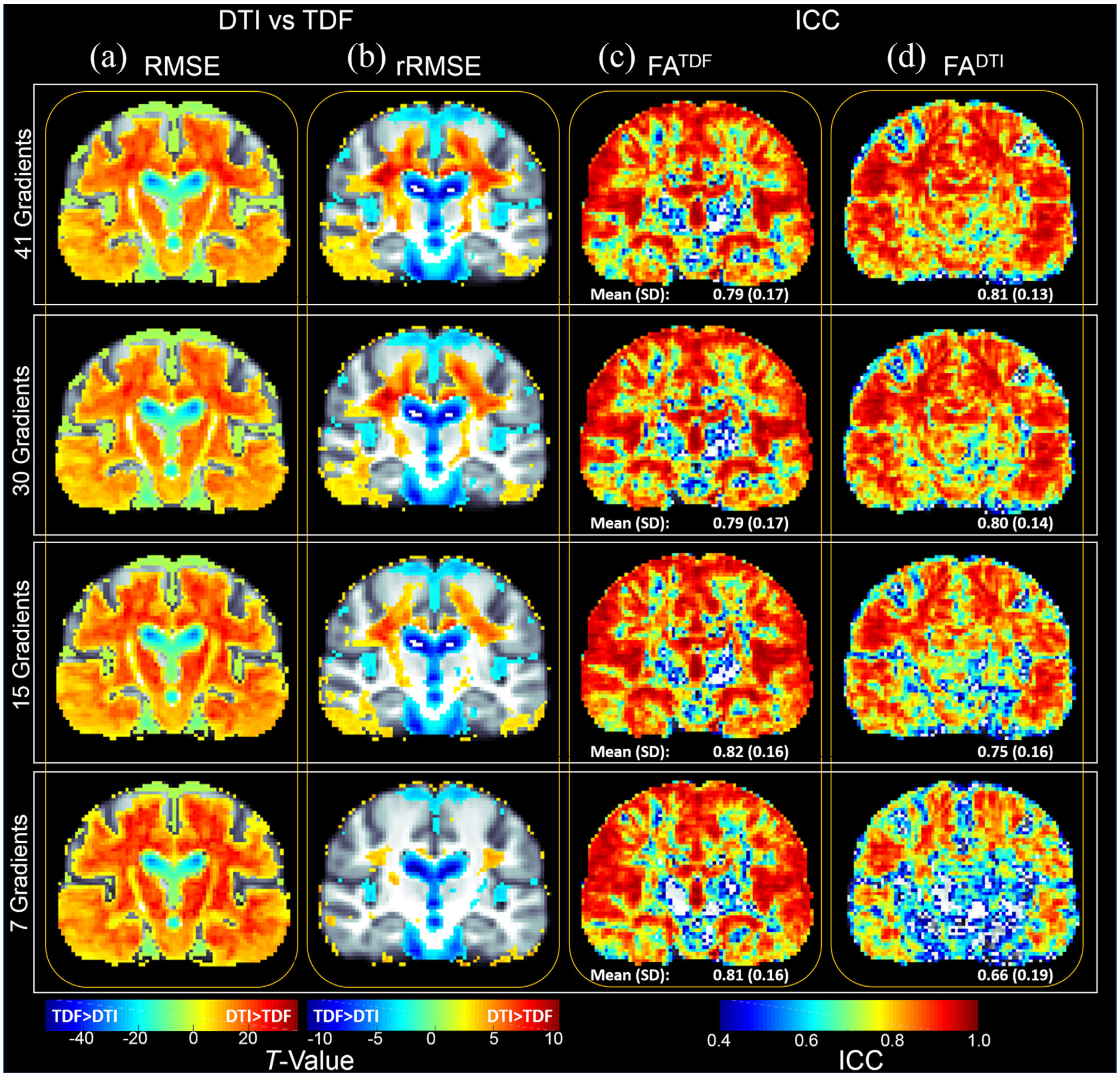

FIG. 5. Statistical differences in reliability between TDF and DTI models. (**a**) *t* maps in regions where the RMSE maps of the TDF and DTI model fit in 53 healthy controls are significantly different reveal higher error for DTI (positive association) throughout the tissue (red) regardless of angular resolution (FDR critical *P* value for 41 gradients = 0.041, 30 gradients = 0.041, 15 gradients = 0.042, and 7 gradients = 0.043). (**b**) *t* maps in regions where the rRMSE maps of the TDF and DTI model fit, trained on 33 healthy controls' baseline scans and tested on 3-month follow-up scans, are significantly different reveal higher error for DTI (positive association) in the tissue (red), particularly in regions of known crossing fibers (FDR critical *P* value for 41 gradients = 0.024, 30 gradients = 0.021, 15 gradients = 0.017, and 7 gradients = 0.001); the TDF model shows higher error only in cerebrospinal fluid. (**c,d**) ICC maps in regions with a significant ICC between baseline and 3-month follow-up (c) FA^{TDF} maps (FDR critical *P* value for 41 gradients = 0.049, 30 gradients = 0.049, 15 gradients = 0.049, and 7 gradients = 0.049) and (d) FA^{DTI} maps (FDR critical *P* value for 41 gradients = 0.050, 30 gradients = 0.050, 15 gradients = 0.049, and 7 gradients = 0.047). The mean ICC and standard deviation (SD) of the ICC across all voxels are reported below each mapped coronal slice.

previously proposed by Jian et al. (47), does not impose the same anisotropy profile on all fiber compartments. This may lead to better estimates if there are higher levels of uncertainty in the data, such as may arise with low resolution data.

Furthermore, FA^{TDF} may also help to interpret apparent increases in FA^{DTI} found in disease. In many contexts, lower FA is hypothesized to reflect impairment. However, relative increases in FA have been reported in FA^{DTI} studies of AD, which may reflect a selective sparing or selective degeneration of one of the pathways in a region with crossing fibers (48). However, without histologic data, we cannot be certain whether selective degeneration or increased integrity—or some combination of both—is driving higher FA^{DTI} values in a neuroimaging study. FA^{TDF}, on the other hand, takes into account crossing fiber compartments. A relatively higher FA may more consistently reflect healthier tissue, whereas lower FA more consistently reflects deficits, making the direction of associations easier to interpret. Across analyses, we found that FA^{TDF} showed fewer "contrary to hypothesis" regions (i.e., higher FA associated with greater deficits). Across all statistical tests and angular resolutions, compared with FA^{TDF}, FA^{DTI} showed both a higher absolute number of these types of significant voxels and a higher percentage relative to the total number of significant voxels (~5%–15% of voxels versus < 0.5% with FA^{TDF}), suggesting that FA^{TDF} may in fact be resolving crossing fibers.

Analyses of test/retest reliability and model fit showed that the TDF was quite reliable and robust in regions that showed disease effects in this analysis. Some instability in test/retest reliability is to be expected when using the ADNI dataset; the scans were performed 3 months apart, and the healthy control participants were elderly (mean age, 72.8 ± 6.5 y). Furthermore, these individuals may have exhibited some biological aging and WM deterioration, even over the 3-month interscan interval. All registrations were visually evaluated, but age-related changes and minor geometric miscalibration of the scanner may have also contributed to minor discrepancies in alignment between two scans from the same subject, further contributing to both the final test/retest ICC and rRMSE measures in both the DTI and TDF models.

A previous study also showed that FA^{TDF} was a more stable metric with decreasing spatial resolution, whereas FA^{DTI} values decreased more rapidly due to more fiber incoherence and greater partial voluming in larger voxels (49). However, further analyses of FA^{TDF} limitations on a wider range of diffusion protocols and comparisons of performance to numerous other proposed scalar metrics are necessary. In addition to FA, there is also a growing interest in assessing complementary diffusivity metrics, including mean diffusivity, axial diffusivity, and radial diffusivity. Because FA is an inherently normalized measure and diffusivity metrics are not, future work is necessary to define analogous measures within the TDF framework.

Multishell and other diffusion spectrum MRI or q-space techniques may ultimately outperform tensor model metrics, but they are often less feasible given the time constraints on dMRI protocols in clinical settings, as well as for recovering information from valuable legacy data. The TDF model may ultimately allow us to take advantage of such available clinical quality diffusion data with more sensitivity and fewer limitations than the classic DTI model.

APPENDIX

As the probability distribution we fit to the tensors, $P(D(\theta, \lambda))$, is defined as a nonparametric distribution, we sampled the tensor space to solve the optimization problem. As in Leow et al. (13), we set $\lambda_2 = \lambda_3$ and $\lambda_1 \geq \lambda_2$, thus reducing the search of tensors to 2 eigenvalues and a principal eigenvector direction. The cost function could be rewritten (up to a constant multipier S_0) as

$$\begin{aligned} I[P(D(\theta,\lambda))] &= \textstyle\sum_i \left(S_{obs}(q_i) - \sum_{k=1}^{M} P(D_k)\exp(-q_i^T \mathrm{D}_k \mathrm{q}_i) \right)^2 \\ &= \frac{1}{2} x^T (2FF^T)\, x - x^T (2Fs) + || s ||^2 \end{aligned} \qquad [A1]$$

where $x \in R^M$ is the vector of probabilities $x_i = P(D_i)$, $i = \overline{1, M}$ (where M is the number of elements in sampling); $s \in R^N$ is the vector of observed intensities of the DW measures (where N is the number of DW scans); and $F \in R^{M \times N}$ is the matrix of elements $F_{ij} = exp(-q_j^T D_i q_j)$.

Clearly, we search for a vector x that minimizes the cost function with two constraints:

$$x_i > 0, \ \ i = \overline{1, M}$$
$$\sum_{i=1}^{M} x_i = 1 \quad ,$$

which lends itself to a classic quadratic programming (QP) problem (50). By definition, the matrix $H = 2FF^T$ is positive semidefinite, which means that the problem is convex. However, by construction, the rank of the matrix $\mathbf{H}$ cannot exceed N (the number of observations). Therefore, if the tensor space sampling has more than N points, the problem has multiple optimal solutions. The original gradient descent approach described by Leow et al. (13) used the substitution $P(D) = exp\big(R(D)\big)$ to meet the constraint $P(D_i) > 0$. It also used a feasible-direction gradient descent method, projecting the steepest descent direction onto the constraint $\int P(D)dD = 1$. Even so, as long as P is sought as a nonparametric distribution based on a sampling at predefined grid points, multiple optimal solutions still remain a problem. Instead, we used the primal-dual predictor-corrector interior-point method (51) to solve the optimization problem. The method that we used is one of the interior-point methods family, which converges to a unique solution from the feasible interior region to the optimum, following the central path (52). Generally, interior-point methods solve the problem

$$min_x \left[c^T x + \frac{1}{2} x^T H x - \mu \sum_{j=1}^{M} ln \ x_j \right]$$

given (in our case) $H = 2FF^T$, $c = -2Fs$, and the constraint $e^T x = 1$ and $x_i = P(D_i) > 0$ as defined above ($e_i = 1, i = \overline{1, M}$). Starting with large μ, this functional is being decreased on every step, enforcing the solution to be close to the line $x_1 = x_2 = \ldots = x_M$, which is a minimizer for the $(-\mu \sum_{j=1}^{M} ln \ x_j)$ term. A QP solver implemented as compiled C++ code (http://sigpromu.org/quadprog/) was used for solving the minimization problem.

Numerical Implementation Details

The following sampling scheme was chosen for the tensor space: $\lambda_1 = [0.2 \ \ 0.4 \ \ \ldots \ \ 2.0]$, $\lambda_2 = [0.2 \ \ 0.4 \ \ \ldots \ \ \lambda_1]$, resulting in 55 sampling points for the lambda combinations. Principal eigenvectors were sampled at two resolution levels as centers of faces of half an icosahedron (to represent the hemisphere), resulting in 10 directions at the low-resolution level and 40 directions at the higher-resolution level (by subdividing each icosahedral face into four new ones). A freely available set of functions (https://www.mathworks.com/matlabcentral/fileexchange/37004-suite-of-functions-to-perform-uniform-sampling-of-a-sphere) was used to build and subdivide an icosahedron.

The algorithm may be summarized as follows:

1. Pre-compute matrices F, H.
2. For each voxel:
    a. Compute the vector $c = -2Fs$ (given s – vector of DW observations in voxel).
    b. Solve the QP problem (Eq. A1).
    c. Compute the TOD as $TOD(\theta) = \int_{\lambda} P\left(D(\theta, \lambda)\right) d\lambda$.
    d. For directions where the value of the TOD exceeds the threshold (as implemented in Leow et al. (13), but set here to $1/10 = 0.1$), upsample – replace each low-resolution direction with four corresponding higher-resolution directions to fine-tune the tensor orientation probabilities.
    e. Solve QP again only for the higher-resolution directions.
    f. Compute higher-resolution output metrics (FA^{TDF}) as well as RMSE.

ACKNOWLEDGMENTS

Data collection and sharing for this project was funded by the ADNI (National Institutes of Health Grant U01 AG024904) and DOD ADNI (Department of Defense award number W81XWH-12-2-0012). The ADNI is funded by the National Institute on Aging, the National Institute of Biomedical Imaging and Bioengineering, and through generous contributions from the following: Alzheimer's Association; Alzheimer's Drug Discovery Foundation; Araclon Biotech; BioClinica, Inc.; Biogen Idec Inc.; Bristol-Myers Squibb Company; Eisai Inc.; Elan Pharmaceuticals, Inc.; Eli Lilly and Company; EuroImmun; F. Hoffmann-La Roche Ltd and its affiliated company Genentech, Inc.; Fujirebio; GE Healthcare; IXICO Ltd.; Janssen Alzheimer Immunotherapy Research & Development, LLC.; Johnson & Johnson Pharmaceutical Research & Development LLC.; Medpace, Inc.; Merck & Co., Inc.; Meso Scale Diagnostics, LLC.; NeuroRx Research; Neurotrack Technologies; Novartis Pharmaceuticals Corporation; Pfizer Inc.; Piramal Imaging; Servier; Synarc Inc.; and Takeda Pharmaceutical Company. The Canadian Institutes of Health Research provides funds to support ADNI clinical sites in Canada. Private sector contributions are facilitated by the Foundation for the National Institutes of Health (www.fnih.org). The grantee organization is the Northern California Institute for Research and Education, and the study is coordinated by the Alzheimer's Disease Cooperative Study at the University of California–San Diego. ADNI data are disseminated by the Laboratory for Neuro Imaging at the University of Southern California. Funding for the ENIGMA Center for Worldwide Medicine Imaging and Genomics is provided as part of the BD2K Initiative under grant number U54 EB020403 to support big data analytics.

Many of the ADNI investigators contributed to the design and implementation of ADNI and/or provided data, but most of them did not participate in this analysis or help write this report. A complete list of ADNI investigators is available at https://adni.loni.usc.edu/wp-content/uploads/how_to_apply/ADNI_Acknowledgement_List.pdf.

REFERENCES

1. Descoteaux M, Poupon C. Diffusion-weighted MRI. In: Brahme A, editor. Comprehensive biomedical physics. Amsterdam: Elsevier; 2012;3: 81–97.
2. Stejskal EO, Tanner JE. Spin diffusion measurements: spin echoes in the presence of a time-dependent field gradient. J Chem Phys 1965; 42:288–292.
3. Basser PJ, Mattiello J, LeBihan D. MR diffusion tensor spectroscopy and imaging. Biophys J 1994;66:259–267.
4. Behrens TE, Berg HJ, Jbabdi S, Rushworth MF, Woolrich MW. Probabilistic diffusion tractography with multiple fibre orientations: what can we gain? Neuroimage 2007;34:144–155.
5. Descoteaux M, Deriche R, Knosche TR, Anwander A. Deterministic and probabilistic tractography based on complex fibre orientation distributions. IEEE Trans Med Imaging 2009;28:269–286.
6. Weston PSJ, Simpson IJA, Ryan NS, Ourselin S, Fox NC. Diffusion imaging changes in grey matter in Alzheimer's disease: a potential marker of early neurodegeneration. Alzheimer's Research & Therapy 2015;7:47.
7. Nir TM, Jahanshad N, Villalon-Reina JE, et al. Effectiveness of regional DTI measures in distinguishing Alzheimer's disease, MCI, and normal aging. Neuroimage Clin 2013;3:180–195.
8. Nir TM, Villalon-Reina JE, Prasad G, et al. Diffusion weighted imaging-based maximum density path analysis and classification of Alzheimer's disease. Neurobiol Aging 2015;36(suppl 1):S132–S140.
9. Tuch DS. Q-ball imaging. Magn Reson Med 2004;52:1358–1372.
10. Tournier JD, Calamante F, Gadian DG, Connelly A. Direct estimation of the fiber orientation density function from diffusion-weighted MRI data using spherical deconvolution. Neuroimage 2004;23:1176–1185.
11. Wedeen VJ, Hagmann P, Tseng WY, Reese TG, Weisskoff RM. Mapping complex tissue architecture with diffusion spectrum magnetic resonance imaging. Magn Reson Med 2005;54:1377–1386.
12. Zhang H, Schneider T, Wheeler-Kingshott CA, Alexander DC. NODDI: practical in vivo neurite orientation dispersion and density imaging of the human brain. Neuroimage 2012;61:1000–1016.
13. Leow AD, Zhu S, Zhan L, et al. The tensor distribution function. Magn Reson Med 2009;61:205–214.
14. Alexander DC. A general framework for experiment design in diffusion MRI and its application in measuring direct tissue-microstructure features. Magn Reson Med 2008;60:439–448.
15. Barazany D, Basser PJ, Assaf Y. In vivo measurement of axon diameter distribution in the corpus callosum of rat brain. Brain 2009;132: 1210–1220.
16. Alexander DC, Hubbard PL, Hall MG, et al. Orientationally invariant indices of axon diameter and density from diffusion MRI. Neuroimage 2010;52:1374–1389.
17. Nir TM, Zavaliangos-Petropulu A, Jahanshad N, et al., editors. Diffusion Tensor Distribution Function Metrics Boost Power to Detect Defecits in Alzhemier's Disease. Presented at IEEE 13th International Symposium on Biomedical Imaging (ISBI); Prague, Czech Republic; April 13–16, 2016.
18. Berg L. Clinical Dementia Rating (CDR). Psychopharmacol Bull 1988; 24:637–639.
19. Leow AD, Yanovsky I, Chiang MC, et al. Statistical properties of Jacobian maps and the realization of unbiased large-deformation nonlinear image registration. IEEE Trans Med Imaging 2007;26:822–832.
20. Zhan L, Leow AD, Jahanshad N, et al. How does angular resolution affect diffusion imaging measures? Neuroimage 2010;49:1357–1371.
21. Zhan L, Leow AD, Zhu S, et al. A novel measure of fractional anisotropy based on the tensor distribution function. Med Image Comput Comput Assist Interv 2009;12:845–852.
22. Benjamini Y, Hochberg Y. Controlling the false discovery rate: a practical and powerful approach to multiple testing. J R Stat Soc Series B Stat Methodol 1995:289–300.

23. Aganj I, Lenglet C, Sapiro G, Yacoub E, Ugurbil K, Harel N. Reconstruction of the orientation distribution function in single- and multiple-shell q-ball imaging within constant solid angle. Magn Reson Med 2010;64:554–566.
24. Avants BB, Tustison NJ, Song G, Cook PA, Klein A, Gee JC. A reproducible evaluation of ANTs similarity metric performance in brain image registration. Neuroimage 2011;54:2033–2044.
25. Smith SM, Zhang Y, Jenkinson M, et al. Accurate, robust, and automated longitudinal and cross-sectional brain change analysis. Neuroimage 2002;17:479–489.
26. Cohen J. Statistical power analysis for the behavioral sciences. Hillsdale, NJ: L. Erlbaum Associates; 1988.
27. Schmaal L, Hibar DP, Samann PG, et al. Cortical abnormalities in adults and adolescents with major depression based on brain scans from 20 cohorts worldwide in the ENIGMA Major Depressive Disorder Working Group. Mol Psychiatry 2016. doi: 10.1038/mp.2016.60.
28. van Erp TG, Hibar DP, Rasmussen JM, et al. Subcortical brain volume abnormalities in 2028 individuals with schizophrenia and 2540 healthy controls via the ENIGMA consortium. Mol Psychiatry 2016; 21:585.
29. Hibar DP, Westlye LT, van Erp TG, et al. Subcortical volumetric abnormalities in bipolar disorder. Mol Psychiatry. 2016;21:1710–1716.
30. Rokem A, Yeatman JD, Pestilli F, et al. Evaluating the accuracy of diffusion MRI models in white matter. PLoS One 2015;10:e0123272.
31. Pestilli F, Yeatman JD, Rokem A, Kay KN, Wandell BA. Evaluation and statistical inference for human connectomes. Nat Methods 2014; 11:1058–1063.
32. Oishi K. MRI atlas of human white matter. Amsterdam: Elsevier/Academic Press; 2011.
33. Delbeuck X, Van der Linden M, Collette F. Alzheimer's disease as a disconnection syndrome? Neuropsychol Rev 2003;13:79–92.
34. Oishi K, Mielke MM, Albert M, Lyketsos CG, Mori S. DTI analyses and clinical applications in Alzheimer's disease. J Alzheimers Dis 2011;26(suppl 3):287–296.
35. Toga AW, Thompson PM. Connectomics sheds new light on Alzheimer's disease. Biol Psychiatry 2013;73:390–392.
36. Jack CR Jr, Barnes J, Bernstein MA, et al. Magnetic resonance imaging in Alzheimer's Disease Neuroimaging Initiative 2. Alzheimers Dement 2015;11:740–756.
37. Xie S, Xiao JX, Gong GL, et al. Voxel-based detection of white matter abnormalities in mild Alzheimer disease. Neurology 2006;66:1845–1849.
38. Canu E, McLaren DG, Fitzgerald ME, et al. Microstructural diffusion changes are independent of macrostructural volume loss in moderate to severe Alzheimer's disease. J Alzheimers Dis 2010;19:963–976.
39. Bozzali M, Cercignani M, Sormani MP, Comi G, Filippi M. Quantification of brain gray matter damage in different MS phenotypes by use of diffusion tensor MR imaging. AJNR Am J Neuroradiol 2002;23: 985–988.
40. Cercignani M, Bozzali M, Iannucci G, Comi G, Filippi M. Magnetisation transfer ratio and mean diffusivity of normal appearing white and grey matter from patients with multiple sclerosis. J Neurol Neurosurg Psychiatry 2001;70:311–317.
41. Chiapponi C, Piras F, Piras F, Fagioli S, Caltagirone C, Spalletta G. Cortical grey matter and subcortical white matter brain microstructural changes in schizophrenia are localised and age independent: a case-control diffusion tensor imaging study. PLoS One 2013;8: e75115.
42. Whitwell JL, Avula R, Senjem ML, et al. Gray and white matter water diffusion in the syndromic variants of frontotemporal dementia. Neurology 2010;74:1279–1287.
43. Kantarci K, Petersen RC, Boeve BF, et al. DWI predicts future progression to Alzheimer disease in amnestic mild cognitive impairment. Neurology 2005;64:902–904.
44. Muller MJ, Greverus D, Dellani PR, et al. Functional implications of hippocampal volume and diffusivity in mild cognitive impairment. Neuroimage 2005;28:1033–1042.
45. Hugenschmidt CE, Peiffer AM, Kraft RA, et al. Relating imaging indices of white matter integrity and volume in healthy older adults. Cereb Cortex 2008;18:433–442.
46. Nir TM, Jahanshad N, Toga AW, et al. Connectivity network measures predict volumetric atrophy in mild cognitive impairment. Neurobiol Aging 2015;36(suppl 1):S113–S120.
47. Jian B, Vemuri BC, Ozarslan E, Carney PR, Mareci TH. A novel tensor distribution model for the diffusion-weighted MR signal. Neuroimage 2007;37:164–176.
48. Douaud G, Jbabdi S, Behrens TE, et al. DTI measures in crossing-fibre areas: increased diffusion anisotropy reveals early white matter alteration in MCI and mild Alzheimer's disease. Neuroimage 2011;55: 880–890.
49. GadElkarim JJ, Zhan L, Yang SL, et al., editors. TDF-TRACT: Probabilistic tractography using the tensor distribution function. 2011 IEEE International Symposium on Biomedical Imaging: From Nano to Macro; Chicago, IL; March 30–April 2, 2011.
50. Nocedal J, Wright S. Numerical optimization. New York, NY; Springer Science & Business Media; 2006. 664 p.
51. Mehrotra S. On the Implementation of a Primal-Dual Interior Point Method. SIAM J Optim 1992;2:575–601.
52. Gondzio J. Interior point methods 25 years later. Eur J Oper Res 2012; 218:587–601.